Applied Physics Letters ARTICLE scitation.org/journal/apl

Stoichiometry-dependent surface electronic structure of $SrTiO_3$ films grown by hybrid molecular beam epitaxy

Cite as: Appl. Phys. Lett. **120**, 121604 (2022); doi: 10.1063/5.0082636
Submitted: 16 December 2021 · Accepted: 11 March 2022 ·
Published Online: 24 March 2022

Dooyong Lee,[1,a)] Fengdeng Liu,[1] Tristan K. Truttmann,[1] Scott A. Chambers,[2,a)] and Bharat Jalan[1,a)]

AFFILIATIONS

[1]Department of Chemical Engineering and Materials Science, University of Minnesota-Twin Cities, Minneapolis, Minnesota 55455, USA

[2]Physical and Computational Sciences Directorate, Pacific Northwest National Laboratory, Richland, Washington 99352, USA

[a)]**Authors to whom correspondence should be addressed:** dylee@umn.edu; sa.chambers@pnnl.gov; and bjalan@umn.edu

ABSTRACT

We investigate the surface electronic structure of $SrTiO_3$ (STO) films grown by a hybrid molecular beam epitaxy that are both stoichiometric and nonstoichiometric by means of x-ray photoelectron spectroscopy and electron energy loss spectroscopy. Increasing the fraction of the surface that is terminated with an SrO layer is correlated with a decrease in the chemical potential whereby the valence band maximum moves closer to the Fermi level, but without a significant change in the bandgap. Inasmuch as SrO-terminated STO (001) has previously been shown to act as an electron scavenger in which carriers from the bulk are trapped, we argue that the high fraction of SrO in the terminal layer is what lowers the chemical potential in Sr-rich STO. Our experimental results provide important insights into various physical phenomena that can occur on STO (001) surfaces and their effect on bulk electronic properties.

$SrTiO_3$ (STO) is of interest for both fundamental understanding and applications in oxide electronics and has received considerable attention as a result. STO is also widely used as a substrate and a bottom layer for heterojunctions, some of which have exhibited unexpected physical phenomena. For example, the heavily studied $LaAlO_3$/$SrTiO_3$ heterostructure exhibits a two-dimensional electron gas (2DEG) with an insulator-to-metal transition (IMT) as well as ferromagnetism and superconductivity.[1–3] These exotic phenomena have been explained by electronic reconstruction and quantum confinement of electrons owing to the polar discontinuity at the interface.[4,5] In addition, oxygen vacancies and interdiffusion of cations at the interface of the heterostructure can induce exotic phenomena by causing electronic reconstruction as well.[6–8]

STO surfaces also exhibit unusual and interesting behavior. For example, an in-gap state was detected by x-ray photoelectron spectroscopy (XPS) on the surface of electron-doped STO(001).[9–11] This state was concluded to originate from delocalization of electrons generated by doping and oxygen vacancy creation. Additionally, a 2DEG has also been shown to form on a SrO-terminated STO(001) surface after exposure to ultraviolet light.[12] These results demonstrate that surface composition is an important factor in driving interesting physical phenomena.

To understand the correlations between surface chemical state and the corresponding physical properties, it is of interest to examine surface electronic structure as film stoichiometry and surface termination are varied. Chambers and Sushko[13] investigated the work function of SrO- and TiO_2-terminated STO films using angle-integrated ultraviolet photoelectron spectroscopy (UPS). The work function of the SrO-terminated STO film was lower than expected based on first-principles calculations. These authors suggested that the discrepancy can be associated with the small electronic affinity induced by defects on the SrO-terminated surface. Such defects also appear to be important in the formation of a 2DEG on the SrO-terminated STO surface.[12] Pal *et al.*[11] found an IMT on $SrTiO_{3-x}$ film surfaces using XPS. The IMT was generated by the evolution of the in-gap state with increasing annealing temperatures, which in turn results in itinerant electrons due to oxygen vacancy formation. However, despite much effort to understand the electronic structure of STO surfaces, there are very little done to understand the relationship between the surface composition and electronic structure in STO.

Here, we investigate the electronic structure of homoepitaxial STO(001) films grown by hybrid molecular beam epitaxy (*h*MBE) as the film stoichiometry is varied from Sr-rich to stoichiometric to Ti-

rich. The *h*MBE method enables state-of-the-art control over stoichiometry by means of growth window utilization.[14,15] We use XPS to determine surface termination, composition, and valence band (VB) properties. Additionally, we have probed the electronic structure of the conduction band (CB) by means of electron energy loss spectroscopy (EELS), using the O 1*s* photoelectron as our probe.[16,17] Using XPS and XPS-derived EELS simultaneously, we find that increasing the fraction of the terminal layer that consists of SrO decreases the chemical potential [i.e., moves the valence band closer to the Fermi level (E_F)] without a measurable change in the bandgap. Indeed, our results point to the composition of the terminal layer as the driver behind chemical potential evolution as a function of overall film stoichiometry.

15 nm STO films with different compositions were grown on STO(001) substrates using *h*MBE [see Fig. 1(d)] at a substrate temperature of 900 °C. Sr was evaporated from an effusion cell. Activated oxygen was supplied using a radio frequency oxygen plasma source at an oxygen pressure of 5×10^{-6} Torr. A metal-organic chemical precursor for Ti, titanium tetra isopropoxide (TTIP, 99.999%, Sigma-Aldrich, USA), was used as a Ti-source. To vary the film stoichiometry in a controllable way, the beam equivalent pressure (BEP) of Sr was fixed at 8.50×10^{-8} Torr by keeping the Sr cell temperature at 475 °C while the BEP of TTIP was set at 5.2×10^{-6}, 6.1×10^{-6}, 6.9×10^{-6}, and 8.7×10^{-6} Torr, leading to TTIP/Sr BEP ratios of 6.14, 7.14, 8.19, and 10.28, respectively. The films were cooled to 250 °C in the presence of oxygen plasma in order to suppress oxygen vacancy formation. The surface structure and morphology of the STO films were investigated by *in situ* reflection high-energy electron diffraction (RHEED, Staib Instruments) and *ex situ* atomic force microscopy (AFM, Bruker), respectively. Structural properties and the lattice parameters of STO films were determined from high-resolution x-ray diffraction (XRD) (SmartLab XE, Rigaku) and reciprocal space mapping (RSM) in the vicinity of the (103) substrate peak. XPS (Physical Electronics VersaProbe III) was carried out with a monochromatic Al K_α x-ray source, a pass energy of 55 eV, and an energy step size of 0.1 eV. An argon gas cluster ion beam (Ar-GCIB) with an energy of 1 keV at an incidence angle of 30° was used to clean the surfaces for 30 s prior to XPS scans. The absence of a grounding wire from the film surfaces to the sample holder required the use of a low-energy electron flood gun to compensate the positive photoemission-induced surface charge. The use of the flood gun allowed spectra to be recorded without line shape distortions. However, flood gun usage also resulted in arbitrary binding energies that are typically lower than they would be if the film was grounded due to the accumulation of a net negative charge on the surface. In order to facilitate extraction of physically meaningful binding energies, all spectra were, therefore, shifted so the associated C 1*s* feature from aliphatic carbon on the surface fell at 286.0 eV, the binding energy measured for a properly grounded Nb-doped STO (001) bulk crystal with surface contamination. The measured x-ray photoelectron spectra of the Sr 3*d*, Ti 2*p*, and O 1*s* core-levels were fitted using a combination of Gaussian and Lorentzian (GL) line shapes after subtracting the Shirley background. The O 1*s* EELS were acquired by XPS after cleaning film surfaces for 4 min using

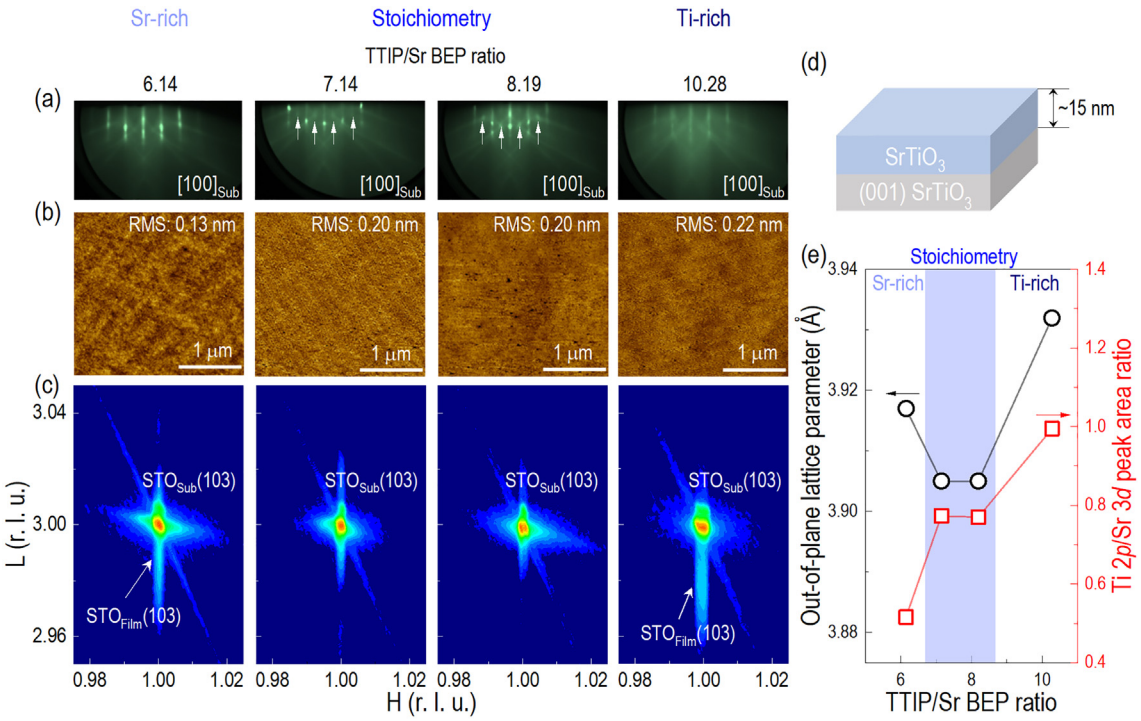

FIG. 1. (a) RHEED patterns along the [100] azimuth and (b) AFM images for STO films with different TTIP/Sr BEP ratios. The white arrows in (a) point to half-order spots indicative of surface reconstruction. (c) RSMs for the STO films near the (103) Bragg peak of the STO substrate. (d) Schematic of the sample structure. (e) Out-of-plane lattice parameters calculated from the RSM results and Ti 2p/Sr 3d peak area ratios determined from the XPS as a function of TTIP/Sr BEP ratio. The blue-shaded region marks the growth window for stoichiometric STO films.

the Ar-GCIB. All O 1*s* EELS were shifted so that the zero-loss peak with the highest intensity was 0 eV. In the O 1*s* EELS, the electron energy loss peak at ∼5 eV was fitted using GL line shapes after the Shirley background subtraction.

Figure 1(a) shows the RHEED patterns along the [100] azimuth of STO films as a function of the TTIP/Sr BEP ratio. All RHEED patterns are streaky and exhibit Kikuchi bands indicating that all films have smooth surface morphology and high crystalline quality.[15] In addition, half-order reconstruction spots are observed for stoichiometric films, i.e., TTIP/Sr BEP ratios of 7.14 and 8.19 [see white arrows in Fig. 1(a)] similar to what has been reported in the literature.[15,18,19] Figure 1(b) shows the corresponding AFM images. The root-mean-square (RMS) roughness ranges from 0.13 to 0.22 nm, indicating that all films have smooth surfaces.

Figure 1(c) shows RSMs near the (103) Bragg peak of STO as a function of the TTIP/Sr BEP ratio. The film peak falls below the substrate peak when the TTIP/Sr BEP ratio is 6.14, indicating a higher out-of-plane lattice parameter in the film. The film and substrate peaks then merge into a single Bragg reflection as the TTIP/Sr BEP ratio increases to 7.14 and 8.19. Finally, the film peak reappears below the substrate peak when the TTIP/Sr BEP ratio = 10.28. RSMs further confirm fully coherent films. Consistent with the RSMs results, the XRD 2θ–ω scans (Fig. S1) show increased lattice parameters for samples with the TTIP/Sr BEP ratio of 6.14 and 10.28 in addition to revealing no phase impurities. Since the lattice parameter of STO is sensitive to cation stoichiometry, the values obtained from XRD can be used to construct a growth window to determine the BEP ratio range over which stoichiometric films grow.[14] Figure 1(e) shows the out-of-plane lattice parameters determined from the RSMs along with the Ti 2*p*/Sr 3*d* peak area ratios obtained from XPS as a function of the TTIP/Sr BEP ratio. Figure 1(e) further reveals that the Ti 2*p*/Sr 3*d* peak area ratios in STO films remain unchanged within the MBE growth window, whereas it varies outside it in agreement with the Sr-rich and Ti-rich growth conditions.

Figures 2(a)–2(c) show Sr 3*d*, Ti $2p_{3/2}$, and O 1*s* core-levels for the STO film set. The dashed lines indicate average binding energies of Sr^{2+} $3d_{5/2}$ (133.7 eV) and Ti^{4+} $2p_{3/2}$ (459.2 eV), and lattice O 1*s* (530.4 eV) features for STO films with TTIP/Sr BEP ratios of 7.14 and 8.19, respectively, which are within the growth window. The Sr 3*d* spectra were fit using two identical spin–orbit (SO) split doublets representing the "surface" layer and the "bulk" layers. The SO splitting was fixed at 1.76 eV, which is appropriate for Sr $3d_{3/2}$ and Sr $3d_{5/2}$.[20,21] Regardless of the cation stoichiometry, all films showed SrO surface features (light green region) in their Sr 3*d* spectra. Surface SrO can generally be attributed to Sr-(OH) adsorbent, and/or the SrO-like secondary phases near the surface.[20,21] Whether the surface SrO is

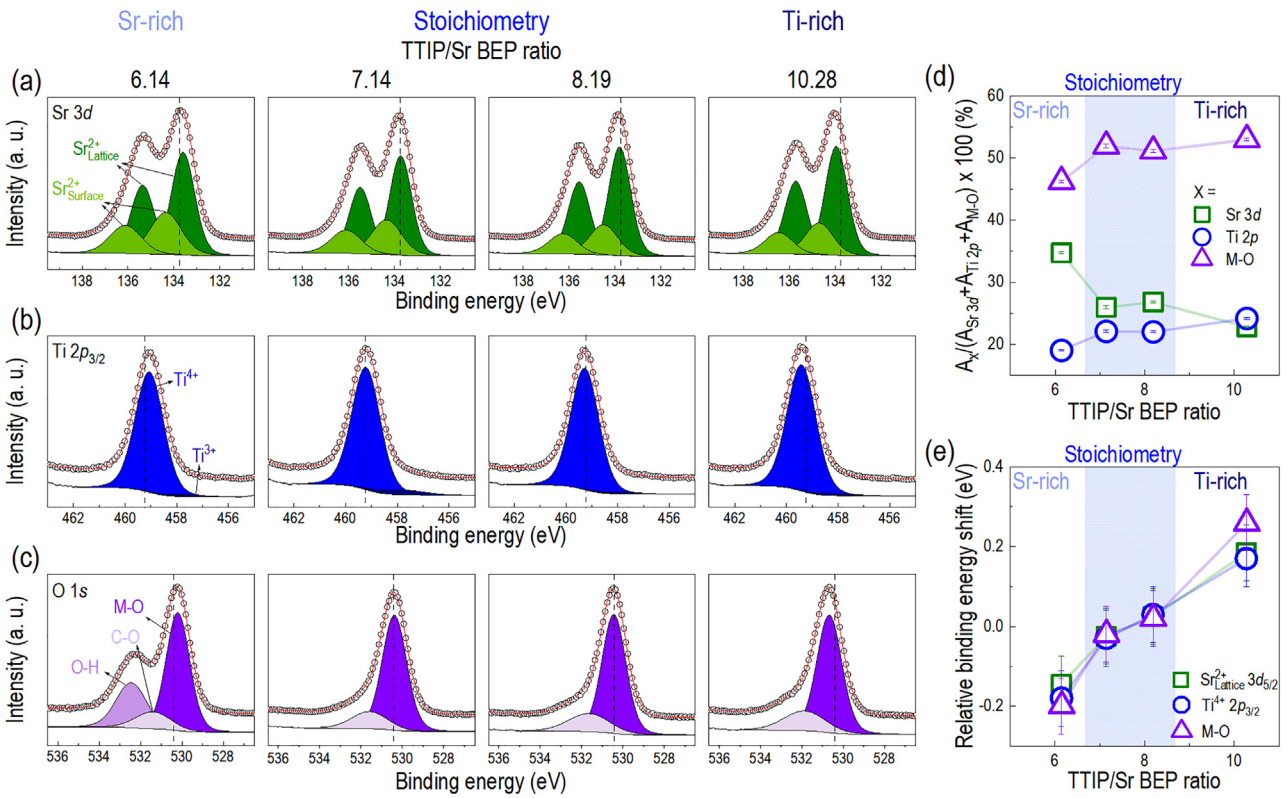

FIG. 2. (a) Sr 3*d*, (b) Ti $2p_{3/2}$, and (c) O 1*s* core-level spectra for STO films prepared with various TTIP/Sr BEP ratios. Vertical dashed lines represent the average binding energies for Sr^{2+} $3d_{5/2}$ (133.7 eV), Ti^{4+} $2p_{3/2}$ (459.2 eV), and lattice O 1*s* (530.4 eV) for the stoichiometric STO films. (d) Core-level peak area ratios $A_x/(A_{Sr\ 3d} + A_{Ti\ 2p} + A_{metal\ oxide}) \times 100$ where x = Sr 3*d*, Ti 2*p* and lattice O 1*s* vs TTIP/Sr BEP ratio. (e) Binding energy shifts relative to those for the stoichiometric films. The blue-shaded region shows the growth window for stoichiometric STO.

from the mixed surface termination or due to a secondary phase was recently investigated by Thapa *et al.*[19] revealing that it is due to an SrO-terminated STO surface. We further confirmed this by measuring the Sr 3*d* spectrum for a TiO_2-terminated Nb-doped STO substrate and showing that the line shape does not show any sign of a second spin–orbit doublet shifted to higher binding energy (Fig. S2), consistent with the previous report.[22] The Ti $2p_{3/2}$ core-level spectra were fit using two features, one for Ti^{4+} and one for Ti^{3+}. The latter corresponds to B-site Ti cations in $SrTiO_3$ screened by electrons in the conduction band from nearby oxygen vacancies.[11] The area under the Ti^{3+} features is ∼2% of the total Ti $2p_{3/2}$ peak area for all films. However, the films are insulating in transport. The O 1*s* core-level spectra were fit to features representing the hydroxyl (O–H) and organic carboxyl (C–O) surface contaminants, along with the metal oxide film lattice (M–O).[23,24] The O–H feature, which was present in all samples, could be largely removed by Ar-GCIB treatment for all but the most Sr-rich film (BEP = 6.14), as confirmed by the corresponding C 1*s* spectra (see Fig. S3) and discussed in more detail below. The detailed fitting results are listed in Table I.

To further characterize the chemical state of the film surfaces, the peak area ratios, defined as $A_x/(A_{Sr\ 3d} + A_{Ti\ 2p} + A_{M-O}) \times 100$, where A is a peak area and x is the identity of the peak (e.g., O 1*s*), along with the binding energy shifts relative to the energies of the films within the growth window, were obtained from the fitting results. The results are shown in Figs. 2(d) and 2(e), respectively. As expected, the total Sr 3*d* peak area decreases and both the Ti 2*p* and O 1*s* peak areas increase with the increasing TTIP/Sr BEP ratio.[14] We note that the peak area ratios do not change within the growth window due to the self-regulating stoichiometry control.[25] Figure 2(e) shows the binding energy shifts of the sub-surface ($Sr_{Lattice}$) Sr $3d_{5/2}$, Ti^{4+} $2p_{3/2}$, and M–O O 1*s* peaks relative to the average of the binding energies for the films with TTIP/Sr BEP ratios of 7.14 and 8.19. The binding energies of all peaks increase with the increase in the TTIP/Sr BEP ratio.

The shift in binding energy for a given element common to two different phases, ΔE_B, is given by the $\Delta E_B = \Delta E_\mu + K\Delta E_Q + \Delta V_M + \Delta E_R$. Here, ΔE_μ is the change in chemical potential, K is the constant of the Coulomb interaction between the valence and core electrons, ΔE_Q is the change in the number of valence electrons, ΔV_M is the change in Madelung potential, and ΔE_R is the change in the core-level potential due to screening.[11] All core-level binding energies increase by similar magnitudes with the increasing TTIP/Sr BEP ratio, which along with the relatively minor changes in the material structure means that ΔV_M and ΔE_R are likely negligible. Furthermore, since there is no significant difference in the valence for either Sr or Ti, $K\Delta E_Q$ is expected to be small. Therefore, we conclude that ΔE_B is dominated by ΔE_μ. As we will see below, there is direct evidence for this conclusion in the VB spectra and the O 1*s* EELS data.

We acquired x-ray excited VB and O 1*s* EELS at the same position on each film, as shown in Figs. 3(a) and 3(b), respectively. The VB spectra show two features at ∼4 and ∼7 eV that originate from non-bonding states and bonding states resulting from hybridization between Ti 3*d* and O 2*p* orbitals, respectively.[11,26,27] However, the two features in the VB spectra are dominated by O 2*p* orbitals because the cross section of the O 2*p* is higher than that of the Ti 3*d*.[11] Both peaks move to high binding energy with the increasing the TTIP/Sr BEP ratio. Interestingly, there is a weak feature between the Fermi level and the O 2*p* peak that appears to reveal an in-gap state for the film with a TTIP/Sr BEP ratio of 6.14, as seen in the inset of Fig. 3(a). The in-gap state has been attributed to the presence of oxygen vacancies in STO.[11,28] However, the Ti 2*p* and O 1*s* core-level spectra show no features related to the oxygen vacancies. As a result, the in-gap feature cannot be attributed to oxygen vacancies. Alternatively, the in-gap state has been assigned to absorbed O–H bound to the STO surface.[29,30] Indeed, the film for which the TTIP/Sr BEP ratio is 6.14 yields the most intense O–H feature in its O 1*s* spectrum. Additionally, the absorbed O–H bonding induces a peak at ∼11 eV [Fig. 3(a)], which has also been observed previously.[29,30]

Figure 3(b) shows the O 1*s* EELS for the STO film set. Inelastic scattering of outgoing photoelectrons can result from plasmon and/or inter-band transitions, leading to distinct features separate from the more intense "no-loss" peak. The first inter-band transition associated with excitation from the top of the VB to the bottom of the CB can be measured when the bandgap is larger than the full-width at half maximum of the no-loss peak.[16,27,31] Accordingly, the O 1*s* spectrum (measured FWHM ≃ 1.4 eV) can be used to investigate the unoccupied electronic states of STO (E_g = 3.25 eV). Figure 3(b) reveals four distinct loss features labeled A, B, C, and D at ∼6 eV, ∼12 eV, ∼20 eV, and ∼30 eV, respectively, along with Ti 2*s* peak at ∼36 eV. The peak A arises from transitions from the largely O 2*p*-derived valence band to the largely Ti 3*d*-derived conduction band. This rather broad feature includes a number of closely spaced dipole-allowed inter-band transitions. As a result, the peak energy of feature A is greater than the bandgap. Nevertheless, the energy of feature A can be used to track changes in the bandgap as the stoichiometry is changed.[16,27,31] The peak B is attributed to the plasmon excitation energy from the O 2*p* band in valence band. The origin of the peak C is not clear, but it may be induced by the excitation of valence or semi-core states. The peak D is associated with the inter-band transitions between the shallow Sr 4*p* and O 2*s* core-level and conduction band.[16] Significantly, none of these loss energies change as the STO stoichiometry is changed. Specifically, the inset of Fig. 3(b) shows no obvious change in the

TABLE I. Binding energy and FWHM of the deconvoluted Sr 3*d*, Ti $2p_{3/2}$, and O 1*s* core-level x-ray photoelectron spectra of STO films with different TTIP/Sr BEP ratios.

	Binding energy (eV)				FWHM (eV)			
TTIP/Sr BEP ratio	Lattice Sr^{2+} $3d_{5/2}$	Surface Sr^{2+} $3d_{5/2}$	Ti^{4+} $2p_{3/2}$	M–O	Lattice Sr^{2+} $3d_{5/2}$	Surface Sr^{2+} $3d_{5/2}$	Ti^{4+} $2p_{3/2}$	M–O
6.14	133.60(7)	134.35(7)	459.06(7)	530.20(7)	1.19	1.55	1.29	1.34
7.14	133.73(7)	134.40(7)	459.21(7)	530.38(7)	1.13	1.49	1.29	1.39
8.19	133.78(7)	134.49(7)	459.27(7)	530.44(7)	1.12	1.44	1.28	1.37
10.28	133.96(7)	134.72(7)	459.41(7)	530.68(7)	1.15	1.38	1.32	1.40

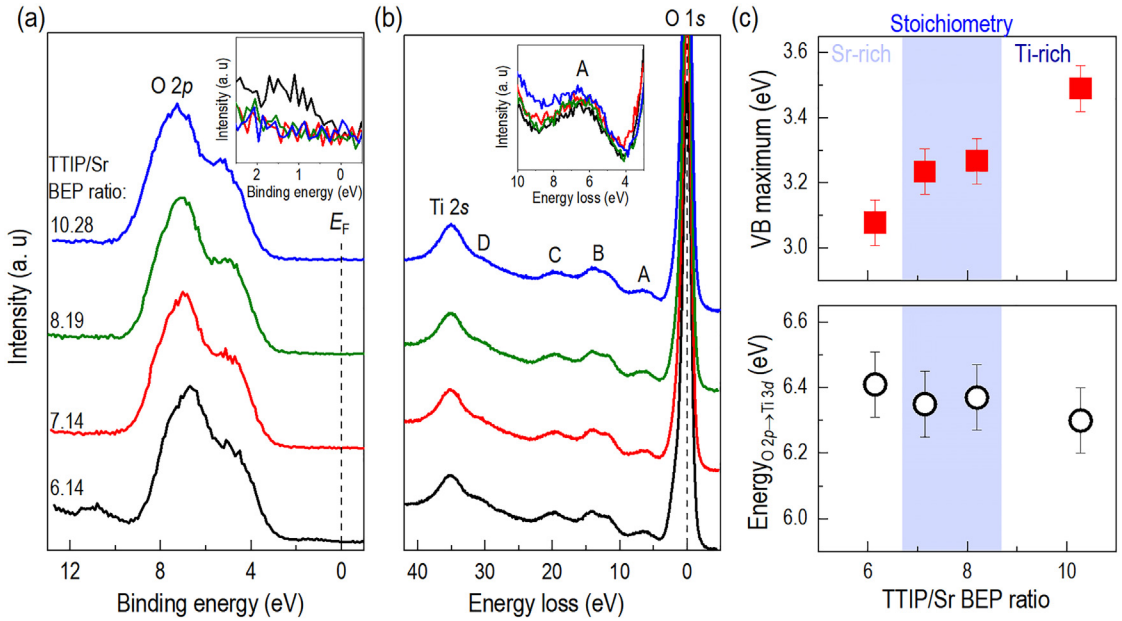

FIG. 3. (a) Valence band spectra and (b) O 1*s* XPS EELS for the STO films with various TTIP/Sr BEP ratios. The insets in (a) and (b) show the valence band spectra near the Fermi level and the peak A in O 1*s* XPS EELS, respectively. (c) Valence band (VB) maximum and inter-band transition energy as a function of the TTIP/Sr BEP ratio. The blue-shaded region shows the growth window for stoichiometric STO films.

position of peak A. We show in the bottom panel of Fig. 3(c) the peak energy for feature A as a function of the TTIP/Sr BEP ratio (see Fig. S4 for the detailed fits).[16] There is no change within experimental error, indicating no change in bandgap with film stoichiometry.

We also extracted the valence band maximum (VBM) values for the film series as shown in the upper panel of Fig. 3(c). We performed linear extrapolations of the leading edges of the VB spectra to the energy axis (see Fig. S5).[26,27] The VBMs for the films with TTIP/Sr BEP ratios of 7.14 and 8.19 are similar to the that of bulk STO (~3.2 eV), as expected for flatband, stoichiometric STO(001). The VBM increases with the increasing TTIP/Sr BEP ratio. Thus, the valence band moves away from the Fermi level even though the

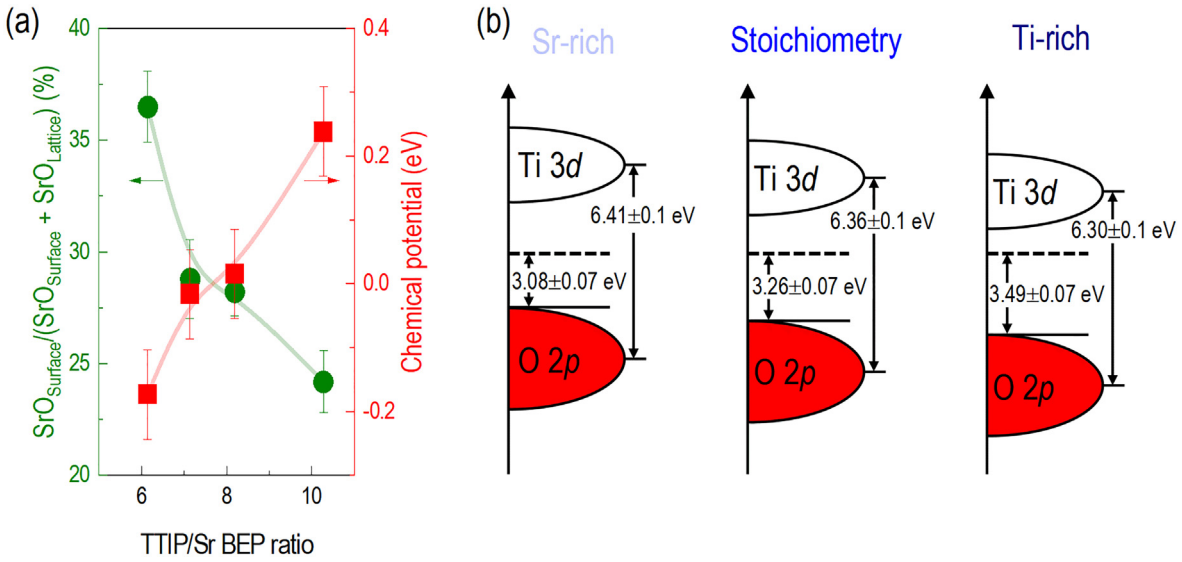

FIG. 4. (a) $SrO_{Surface}/(SrO_{Surface} + SrO_{Lattice})$ and chemical potential shift relative to the chemical potential of two films with a TTIP/Sr BEP ratio of 7.14 and 8.19 as a function of the TTIP/Sr BEP ratio. (b) Schematic of stoichiometry dependent electronic structure of STO based on the experimental results. The chemical potential relative to the VBM clearly increases in going from Sr-rich to Ti-rich, whereas the bandgap remains unchanged within experimental error.

bandgap does not change. The change in VBM is associated with a variation in chemical potential. The chemical potential can be influenced by the O vacancy concentration or variation of the surface electrostatic potential.[11,13] Since there is no evidence for a change in O vacancy concentration, as judged by the magnitude to the Ti^{3+} $2p_{3/2}$ feature [Fig. 2(b)], we attribute the chemical potential change is due to variation of the surface electrostatic potential.

The surface electrostatic potential for STO films can be influenced by surface stoichiometry.[13,19] Our results show that the fraction of the SrO surface-termination layer was found to decrease with the increase in the TTIP/Sr BEP ratio. Figure 4(a) shows the dependences of the $SrO_{Surface}/(SrO_{Surface} + SrO_{Lattice})$ ratio and the chemical potential on the TTIP/Sr BEP ratio. With the increasing TTIP/Sr BEP ratio, the SrO surface-termination fraction decreases and the chemical potential increases.

Based on these experimental results, a plausible stoichiometry-dependent band structure model of STO film is shown in Fig. 4(b). For the Sr-rich STO, the valence band is relatively close to the Fermi level since the $SrO_{surface}$ fraction decreases the chemical potential. In the case of stoichiometric STO, the valence band moves away from the Fermi level due to an increase in chemical potential. Since the Ti-rich STO film has the smallest amount of $SrO_{surface}$, its chemical potential is greatly increased and, thus, the valence band is further away from the Fermi level. These results demonstrate that the surface electronic structure of STO films can be driven by surface properties.

In conclusion, we have investigated the surface electronic structure of STO films with a range of stoichiometry through the XPS valence band spectra and O 1*s* EELS. Structural characterization of the samples is performed by XRD, RHEED, and AFM. It was found that a high fraction of the SrO-terminated surface reduces the chemical potential of STO films but without a change in the bandgap. Since STO is widely in the oxide electronics to stabilize two-dimensional electron gases or other exotic interfacial ground states, our work provides important information to tailor device design based on STO-related heterostructures.

See the supplementary material for wide-angle XRD, Sr 3*d* core-level spectrum for a Nb-doped STO, binding energy calibration, O 1*s* EELS, and Valence band spectra for STO films with different TTIP/Sr BEP ratios.

This work was primarily supported by the U.S. Department of Energy through No. DE-SC002021. F.L. acknowledges support from the Air Force Office of Scientific Research (AFOSR) through Grant Nos. FA9550-19-1-0245 and FA9550-21-1-0025 and partially through NSF No. DMR-1741801. Parts of this work were carried out at the Characterization Facility, University of Minnesota, which receives partial support from National Science Foundation (NSF) through the Materials Research Science and Engineering Center (MRSEC) program under Award No. DMR-2011401. The work at Pacific Northwest National Laboratory (PNNL) was supported by the U.S. Department of Energy, Office of Science, Division of Materials Sciences and Engineering under Award No. 10122 to PNNL.

AUTHOR DECLARATIONS

Conflict of Interest

The authors have no conflicts to disclose.

DATA AVAILABILITY

The data that support the findings of this study are available within the article and its supplementary material.

REFERENCES

[1]A. Ohtomo and H. Y. Hwang, Nature **427**, 423 (2004).
[2]J. A. Bert, B. Kalisky, C. Bell, M. Kim, Y. Hikita, H. Y. Hwang, and K. A. Moler, Nat. Phys. **7**, 767 (2011).
[3]L. Li, C. Richter, J. Mannhart, and R. C. Ashoori, Nat. Phys. **7**, 762 (2011).
[4]H. Y. Hwang, Y. Iwasa, M. Kawasaki, B. Keimer, N. Nagaosa, and Y. Tokura, Nat. Mater. **11**, 103 (2012).
[5]P. R. Willmott, S. A. Pauli, R. Herger, C. M. Schlepütz, D. Martoccia, B. D. Patterson, B. Delley, R. Clarke, D. Kumah, C. Cionca, and Y. Yacoby, Phys. Rev. Lett. **99**, 155502 (2007).
[6]T. Min, W. Choi, J. Seo, G. Han, K. Song, S. Ryu, H. Lee, J. Lee, K. Eom, C.-B. Eom, H. Y. Jeong, Y.-M. Kim, J. Lee, and S. H. Oh, Sci. Adv. **7**, eabe9053 (2021).
[7]K. Song, T. Min, J. Seo, S. Ryu, H. Lee, Z. Wang, S. Choi, J. Lee, C. Eom, and S. H. Oh, Adv. Sci. **8**, 2002073 (2021).
[8]H. Zaid, M. H. Berger, D. Jalabert, M. Walls, R. Akrobetu, I. Fongkaew, W. R. L. Lambrecht, N. J. Goble, X. P. A. Gao, P. Berger, and A. Sehirlioglu, Sci. Rep. **6**, 28118 (2016).
[9]A. Fujimori, I. Hase, M. Nakamura, H. Namatame, Y. Fujishima, Y. Tokura, M. Abbate, F. M. F. de Groot, M. T. Czyzyk, J. C. Fuggle, O. Strebel, F. Lopez, M. Domke, and G. Kaindl, Phys. Rev. B **46**, 9841 (1992).
[10]Y. Ishida, R. Eguchi, M. Matsunami, K. Horiba, M. Taguchi, A. Chainani, Y. Senba, H. Ohashi, H. Ohta, and S. Shin, Phys. Rev. Lett. **100**, 056401 (2008).
[11]P. Pal, P. Kumar, A. V., A. Dogra, and A. G. Joshi, J. Appl. Phys. **116**, 053704 (2014).
[12]S. N. Rebec, T. Jia, H. M. Sohail, M. Hashimoto, D. Lu, Z.-X. Shen, and R. G. Moore, Proc. Natl. Acad. Sci. U. S. A. **116**, 16687 (2019).
[13]S. A. Chambers and P. V. Sushko, Phys. Rev. Mater. **3**, 125803 (2019).
[14]B. Jalan, P. Moetakef, and S. Stemmer, Appl. Phys. Lett. **95**, 032906 (2009).
[15]B. Jalan, R. Engel-Herbert, N. J. Wright, and S. Stemmer, J. Vac. Sci. Technol. A **27**, 461 (2009).
[16]S. Kohiki, M. Arai, H. Yoshikawa, S. Fukushima, M. Oku, and Y. Waseda, Phys. Rev. B **62**, 7964 (2000).
[17]M. Arai, S. Kohiki, H. Yoshikawa, S. Fukushima, Y. Waseda, and M. Oku, Phys. Rev. B **65**, 085101 (2002).
[18]R. B. Comes, P. Xu, B. Jalan, and S. A. Chambers, Appl. Phys. Lett. **107**, 131601 (2015).
[19]S. Thapa, S. R. Provence, D. Jessup, J. Lapano, M. Brahlek, J. T. Sadowski, P. Reinke, W. Jin, and R. B. Comes, J. Vac. Sci. Technol. A **39**, 053203 (2021).
[20]D. Kobayashi, H. Kumigashira, M. Oshima, T. Ohnishi, M. Lippmaa, K. Ono, M. Kawasaki, and H. Koinuma, J. Appl. Phys. **96**, 7183 (2004).
[21]E. J. Crumlin, E. Mutoro, Z. Liu, M. E. Grass, M. D. Biegalski, Y.-L. Lee, D. Morgan, H. M. Christen, H. Bluhm, and Y. Shao-Horn, Energy Environ. Sci. **5**, 6081 (2012).
[22]H. Lim, C. Song, M. Seo, D. Kim, M. Jung, H. Kang, S. Kim, K.-J. Lee, Y. Yu, G. Kim, K.-J. Kim, and B. S. Mun, J. Mater. Chem. C **9**, 13094 (2021).
[23]O. Lobacheva, Y. M. Yiu, N. Chen, T. K. Sham, and L. V. Goncharova, Appl. Surf. Sci. **393**, 74 (2017).
[24]D. Lee, D. Yang, H. Kim, J. Kim, S. Song, K. S. Choi, J.-S. Bae, J. Lee, J. Lee, Y. Lee, J. Yan, J. Kim, and S. Park, J. Phys. Chem. C **124**, 17282 (2020).
[25]A. Prakash, P. Xu, X. Wu, G. Haugstad, X. Wang, and B. Jalan, J. Mater. Chem. C **5**, 5730 (2017).
[26]S. A. Chambers, T. Droubay, T. C. Kaspar, M. Gutowski, and M. van Schilfgaarde, Surf. Sci. **554**, 81 (2004).
[27]G. M. Vanacore, L. F. Zagonel, and N. Barrett, Surf. Sci. **604**, 1674 (2010).
[28]S. A. Chambers, Y. Du, Z. Zhu, J. Wang, M. J. Wahila, L. F. J. Piper, A. Prakash, J. Yue, B. Jalan, S. R. Spurgeon, D. M. Kepaptsoglou, Q. M. Ramasse, and P. V. Sushko, Phys. Rev. B **97**, 245204 (2018).
[29]M. D'Angelo, R. Yukawa, K. Ozawa, S. Yamamoto, T. Hirahara, S. Hasegawa, M. G. Silly, F. Sirotti, and I. Matsuda, Phys. Rev. Lett. **108**, 116802 (2012).
[30]Z. Wang, X. Hao, S. Gerhold, Z. Novotny, C. Franchini, E. McDermott, K. Schulte, M. Schmid, and U. Diebold, J. Phys. Chem. C **117**, 26060 (2013).
[31]S. Miyazaki, AIP Conf. Proc. **550**, 89–96 (2001).